A Novel View on Crystallization and Melting of Semirigid Chain Polymers: The Case of Poly(trimethylene terephthalate)

Dimitri A. Ivanov,*,† Georg Bar,‡ Marcel Dosière,§ and Michel H. J. Koch||

Institut de Chimie des Surfaces et Interfaces, CNRS UPR 9069, Jean Starcky, 15, F-68057, Mulhouse, France, Applied Science & Technology/Analytical Sciences, Dow Olefinverbund GmbH, Schkopau, D16/1.04, Germany, Laboratoire de Physicochimie des Polymères, Université de Mons-Hainaut, Place du Parc, 20, B-7000 Mons, Belgium, and European Molecular Biology Laboratory, Hamburg Outstation, EMBL c/o DESY, Notkestrasse 85, D-22603 Hamburg, Germany

Received July 16, 2008; Revised Manuscript Received October 2, 2008

ABSTRACT: The thermal behavior of semicrystalline polymers constitutes a long-standing problem in polymer crystallization. Although it is widely agreed that the crystal thickness resulting from isothermal crystallization is a sharply selected value, the melting behavior of semicrystalline polymers is very complex. In this work, a combination of high-temperature AFM and time- and temperature-resolved SAXS/WAXS was employed to examine the microstructural evolution during isothermal melt-crystallization and subsequent melting of poly(trimethylene terephthalate). The SAXS data were analyzed in the frame of the generalized paracrystalline lamellar stack model. The crystal thickness remains almost constant and uniform throughout the isothermal crystallization and melting. The crystals squeezed between the thinnest amorphous layers melt first. The reciprocal size of the amorphous regions undergoing transformation scales linearly with temperature. A simple model is proposed, which accounts for this confinement-driven melting by a negative pressure imposed on the crystals by the neighboring amorphous regions.

I. Introduction

One of the long-standing problems in the field of polymer crystallization is related to the understanding the thermal behavior of semicrystalline polymers. Although it is widely agreed that the crystal thickness resulting from isothermal crystallization is a sharply selected value, it remains unclear why the melting behavior of semicrystalline polymers is generally very complex. Thus the melting region of an isothermally crystallized polymer sample can sometimes extend over several tens and even over more than one hundred degrees, while the corresponding DSC curves can exhibit a series of melting and recrystallization peaks.

Much efforts have been devoted in the past to studies of the multiple melting of semirigid chain polymers such as aromatic polyesters (e.g., poly(ethylene terephthalate), poly(butylene terephthalate)) and polyketones (e.g., poly(ether ether ketone), PEEK). To rationalize their thermal behavior, some authors have put forward the so-called melting-recrystallization model[1−23] which explained the appearance of multiple endothermic peaks by a continuous melting-recrystallization process that sets in already a few degrees above the isothermal crystallization temperature. In this model, the complex features in the DSC curves were accounted for by competing endothermic (melting) and exothermic (recrystallization) processes with different kinetics. Such superposition of different processes can also explain why the DSC curves of semirigid chain polymers are rather heating-rate-dependent. It has been also assumed that the driving force of such a continuous recrystallization process is the formation of increasingly thick and perfect crystallites, the thermal stability of which is progressively improved during heating.

In critically reviewing the body of experimental data related to the melting-recrystallization model, it is worth noting that the crystal thickening observed during heating of semirigid chain polymers is often rather limited [e.g., for PEEK see refs 4 and 5]. This raises some doubts as to whether the observed melting behavior can be entirely accounted for by such a small crystal thickness variation. In our previous work, we investigated the evolution of the semicrystalline morphology of isothermally crystallized PEEK during subsequent heating up to the final melting region.[6] A combination of *ex situ* AFM, X-ray scattering and DMTA showed that the presence of large-scale reorganization processes in the semicrystalline structure was paralleled by a substantial variation of the glass transition temperature, T_g, of the interlamellar amorphous regions. Thus, along with the increase of long period upon annealing the sample to an increasingly higher temperature, the T_g of the amorphous phase was decreasing. This indicates that the constraints imposed on the crystals by the neighboring amorphous regions are progressively relaxed on heating. The WAXS (wide-angle X-ray scattering) data[5] accordingly show that the PEEK crystalline lattice parameters decrease upon annealing (i.e., the crystal density increases). Importantly, a comparison of the lattice parameters of PEEK with the corresponding monodisperse short-chain oligomers, which are almost 100% crystalline, reveals that the polymer crystals have a larger cross-sectional area.[7] This provides an additional support to the picture of the semicrystalline structure in which the interlamellar amorphous regions impose substantial mechanical stresses on the crystals.

In the present work, we investigated the crystallization and melting behavior of poly(trimethylene terephthalate), PTT, a relatively recently commercialized polyester, by time- and temperature-resolved SAXS, WAXS, and AFM. The thermal properties of PTT,[8] and its crystallization and melting behavior have been described[9,10] and structure formation in PTT fibers has been investigated using simultaneous synchrotron 2D SAXS (small-angle X-ray scattering) and WAXS.[11] The main motivation of the present work is to use PTT as a model semirigid

* Author to whom correspondence should be addressed. Telephone: +33 3 89 60 87 01. Fax: +33 89 60 87 99. E-mail: dimitri.ivanov@uha.fr.
† Institut de Chimie des Surfaces et Interfaces, CNRS UPR 9069.
‡ Applied Science & Technology/Analytical Sciences, Dow Olefinverbund GmbH.
§ Laboratoire de Physicochimie des Polymères, Université de Mons-Hainaut.
|| European Molecular Biology Laboratory, Hamburg Outstation, EMBL c/o DESY.

10.1021/ma801604a CCC: $40.75
Published on Web 11/06/2008

chain polymer to address the thermodynamics of polymer crystallization.

Particular attention is devoted in the present work to issues related to SAXS data analysis. Although the approach based on the classical one-dimensional correlation and interface distribution function analysis[12] is currently used in most SAXS studies of semicrystalline polymers, the generalized paracrystalline lamellar stack model[13] can yield a more detailed description of the polymer morphology including the size-distribution functions of the amorphous and crystalline phases. This last approach is evidently more laborious as it requires implementing nonlinear multiparameter fitting of the SAXS data.[14,15] However access to the full size-distribution functions, rather than a series of different distribution functions, can open the way to a qualitatively different level of understanding of the processes occurring in the semicrystalline structure during crystallization and melting. Here the results of the fits with the paracrystalline model are compared with the morphological parameters obtained in direct-space by high-temperature AFM imaging.

II. Experimental Section

II.1. Materials and Methods. PTT grade *Corterra* CP509210 with an intrinsic viscosity of 0.92 dL/g in a 60/40 phenol/tetrachloroethane mixture at 30 °C was obtained from Shell Chemical Company in the form of pellets and used without further purification. The samples were dried for 4 h at 130 °C prior to experiments. For SAXS/WAXS studies the pellets were hot-molded in a 1 mm thick copper ring and sealed between two 30 μm thick Al foils.

Time-resolved SAXS/WAXS measurements were performed on the X33 double focusing camera of the EMBL[16] on the storage ring DORIS of the Deutsches Elektronen Synchrotron (DESY) in Hamburg, Germany, using a standard data acquisition system.[17] Experiments at variable temperature were carried out with a Mettler FP-82HT heating stage where the aperture of the window had been enlarged. The temperature calibration of the stage was performed with a thermocouple introduced inside the molded polymer.

Data were collected in 10 s time frames. To improve statistics, the frames were further averaged according to the instantaneous crystallization rate. The norm of the scattering vector, $s = 2(\sin\theta)/\lambda$, where 2θ is the scattering angle and $\lambda = 1.5$ Å, the wavelength of the incident X-rays, was calibrated using 12 diffraction orders of dry calcified rat-tail collagen in the small *s*-region and benzoic acid in the high *s*-region.

The intensities were first normalized by the intensity of the incident X-ray beam measured with an ion chamber and corrected for the detector response using the SAPOKO program.[18] In the second step, the parasitic scattering obtained by fitting an analytical function to the scattering of the heating stage with an empty sample container was subtracted from the data taking into account the sample transmittance, estimated from the atomic linear attenuation coefficients.[19] Finally, the contribution of liquid-like scattering, approximated by a constant in the s-range used (0.002−0.04 Å^{-1}), was subtracted from the SAXS curves.

Atomic Force Microscopy. (AFM) experiments were made with a Nanoscope IIIA MultiMode instrument (Veeco Metrology Group) equipped with a heating accessory. Imaging of the semicrystalline structure of PTT at elevated temperatures (210−220 °C) was performed in He atmosphere employing active tip temperature control[20,21] to ensure the conditions of thermal equilibrium in the tip−sample contact area.

II.2. Data Analysis. *II.2.1. WAXS Curves.* To compute the WAXS crystallinity index, the experimental curves were fit with a sum of gaussians corresponding to each of the crystalline reflections of the PTT lattice plus a broad peak (amorphous halo), which was modeled based on the WAXS data of the PTT melt. To obtain good quality fits the amorphous halo had to be appropriately scaled and shifted laterally to account for the thermal expansion and change in the state of the sample. The crystallinity index ($\alpha_{c,WAXS}$) was then computed from the Lorentz-corrected curves as the ratio of the intensity of the crystalline peaks to the total diffracted intensity.

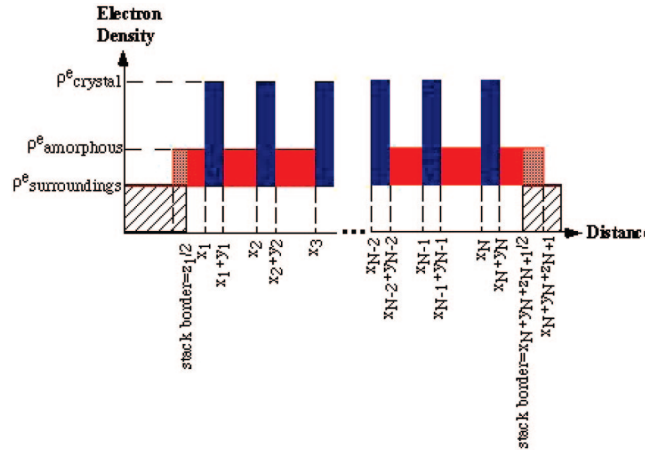

Figure 1. Scheme of a finite paracrystalline lamellar stack containing *N* crystals and $(N + 1)$ interlamellar amorphous regions. The sizes of both regions are distributed according to the functions $h_c(l)$ and $h_a(l)$, respectively. The stack is delimited by two amorphous regions with electron density ρ^e_a located at the boundary with the free melt. The presence of such amorphous zones perturbed by the nearby crystals was previously shown for the case of PET with a selective staining technique.[46] The size of the stack bordering amorphous regions is chosen to be half of those of the ordinary intrastack amorphous regions.

II.2.2. SAXS Curves. were analyzed using the one-dimensional paracrystalline stack model of Hosemann[13] generalized for the case of a finite stack. The data analysis consisting in fitting the entire SAXS curves to the structure factor of such a stack is outlined below. A full account of the model and its implementation for automatic data processing has been given elsewhere.[15]

The finite lamellar stack schematically depicted in Figure 1 is a particular case of a three-phase model, where the semicrystalline structure is not completely space-filling. In this case, the interstack regions are filled with a medium with electron density $\rho^e_{surroundings}$, which, in general, can be different from both the electron density of the crystals, ρ^e_c, and from that of the intrastack amorphous regions, ρ^e_a.

The sizes of the crystals (y_i) and intrastack amorphous regions ($x_{i+1} - x_i - y_i \equiv z_i$) are distributed according to the distribution functions $h_c(l)$ and $h_a(l)$, where *l* stands for the distance. Thus, by construction the lattice incorporates paracrystalline, or second kind, defects. The electron density profile across the stack can be viewed as a sum of the constant intrastack amorphous "background", Π, with electron density ρ_a and an electron density variation due to crystals, $C(l)$, having an amplitude of $(\rho_c - \rho_a)$:

$$\rho(l) = \prod + C(l) \tag{1}$$

The expression for the structure factor of a paracrystalline stack used for fitting the SAXS data reads:

$$I(s) = A\left[I_c(s) + I_B(s) + \left\langle F\left(\prod\right)F^*\left(\prod\right)\right\rangle + 2\left\langle \mathrm{Re}\left[F\left(\prod\right)F^*(C(l))\right]\right\rangle\right] + Bs^2 \tag{2}$$

where I_B and I_c denote the Babinet and non-Babinet terms[13] of the structure factor of crystals, F and F* stand for the Fourier transform and its complex conjugate, Re is the real part of a complex number, A is a normalization constant and B is a constant representing the contribution of the liquid-like background.

The fitting coefficients include the shape parameters of the distribution functions $h_c(l)$, $h_a(l)$, and the constants *A* and *B*, which enter the expression for the Lorentz-modified intensity as a quadratic term. The fits to the generalized Hosemann model were performed

using the Marquardt−Levenberg algorithm[22] by minimizing the χ^2function.

The distributions functions for amorphous and crystalline regions were taken as a normalized sum of truncated gaussians ($h_c(l) = h_a(l) = 0$ for all nonpositive l). For example a single truncated Gaussian representing the distribution of amorphous regions is given by:

$$h_a(l) = \frac{\Theta(l)}{C} \frac{e^{-(1/2)([l-l_0]/\sigma)^2}}{\sqrt{2\pi}\sigma} \tag{3}$$

where $\Theta(l)$ denotes the Heaviside function. The normalization condition applied in this case to $h_a(l)$ results in:

$$C = \frac{1}{2}\left(1 + \mathrm{erf}\left(\frac{l_0}{\sqrt{2}\sigma}\right)\right) \tag{4}$$

The analytical form of the Fourier transform can be written as:

$$F(h_a(l) = e^{2\pi i s l_0} e^{-(2\pi s\sigma)^2/2} \left\{ \frac{1 + \mathrm{erf}\left(\frac{l_0}{\sqrt{2}\sigma} + \frac{2\pi s\sigma}{\sqrt{2}}\right)}{1 + \mathrm{erf}\left(\frac{l_0}{\sqrt{2}\sigma}\right)} \right\} \tag{5}$$

The fitting procedure was first performed with only one Gaussian representing each phase, and the number of constituent gaussians was progressively increased up to three. The results obtained from the fits of the experimental curves with different number of gaussians were compared to evaluate the convergence and reproducibility of the solution. The total number of fitting coefficients equals two for the first Gaussian and three for each additional Gaussian, since, apart from the position of its maximum and the standard deviation, one has to specify its relative amplitude. The crystal thickness distribution was found much narrower than the distributions of amorphous regions and therefore was represented by a single Gaussian. The fits were started using several different initial guesses to check whether the solution was trapped in local minima in the χ^2 function. For example, reasonable initial values for the fitting parameters were estimated from the analysis of the interface distribution function[12] $\gamma'(l)$ defined as the autocorrelation of the first derivative of the electron density profile across the lamellar stack:

$$\gamma''(l) = \frac{d\rho(l)}{dl} \times \frac{d\rho(-l)}{dl} \tag{6}$$

For this estimate, the expansion of $\gamma''(l)$ in a series of different interface distribution functions with alternating signs[23] was used:

$$\gamma''(l) \propto h_c(l) + h_a(l) - 2h_{ac}(l) + h_{aca}(l) + h_{acc}(l) + \ldots \tag{7}$$

It is, however, clear that the thickness distribution functions cannot be found from the $\gamma'(l)$ alone, since they are combined in eq 7.

II.2.3. Quantitative Treatment of AFM Images. This was performed in direct and reciprocal space using methods described previously.[21,25,26] Briefly, after preliminary background correction the images were converted to a binary form. Binarization by simple image thresholding was not always possible because of underlying background undulations and a relatively low contrast. Therefore thresholding was applied to the images treated with a high-pass filter. The morphological features were further sharpened with an image edge detector. The distributions of crystal and amorphous layer thickness were computed on the fully corrected binary images in the direction locally perpendicular to the lamellar edge.

For reciprocal space analysis, the two-dimensional power spectral density function ($P_2(\underline{s})$) was computed from the images ($u(\underline{r})$) up to the critical, or Nyquist, frequency depending upon the experimental sampling interval as:

$$P_2(\underline{s}) \equiv \frac{1}{A}\left|\int_A u(\underline{r}) W(\underline{r}) \exp(2\pi i \underline{s} \cdot \underline{r})\, d^2\underline{r}\right|^2 \tag{8}$$

where A denotes the image area, $W(\underline{r})$ a window function[27] and $\underline{s}$ the 2D reciprocal space vector. The $P_2(\underline{s})$ function was then transformed into the one-dimensional PSD ($P_1(s)$), where s stands for the norm of $\underline{s}$, according to:

$$P_1(s) = (2\pi s)^{-1} \int P_2(\underline{s}')\delta(|\underline{s}'| - s)\, d\underline{s}' \tag{9}$$

III. Results

III.1. Semicrystalline Morphology of Melt-Crystallized PTT. To visualize the time dependent *in situ* structure formation in PTT high temperature AFM imaging was used. The choice of the temperature for such measurements is typically limited to a temperature region close to the final melting point (i.e., on the decreasing branch of the growth rate versus temperature curve) due to the limited AFM imaging rate. The advantage of this approach is that it gives a direct space view of the crystallization process and ensures that the polymer morphology is not modified during subsequent cooling to the temperature of observation, e.g. room temperature.

The first set of high temperature AFM experiments was carried out at a temperature of 210 °C where the formation of a spherulitic band can be observed in detail (Figure 2A). An S-shaped lamellar ribbon at the center of the image nicely reveals the twisted growth mode in which the lamellar bundles display a synchronous rotation about the fast growth axis

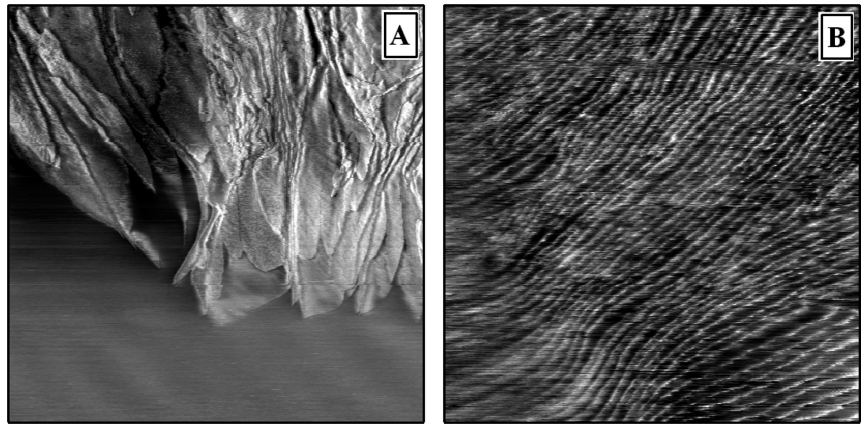

Figure 2. High-temperature tapping mode phase AFM images showing the semicrystalline morphology of PTT during isothermal melt-crystallization at 210 °C. The left image (10 × 10 μm^2) displays the edge of a growing spherulite, which exhibits a banded structure. Formation of the band is visible in the central part of the image where an S-shaped helicoidal lamellar ribbon changes from a flat-on to an edge-on orientation. The right image (600 × 600 nm^2) gives a close view of the lamellar morphology in a part of the spherulite where the lamellae are mainly edge-on. The beginning of the lamellar twist is distinctly seen in the bottom left corner of the image.

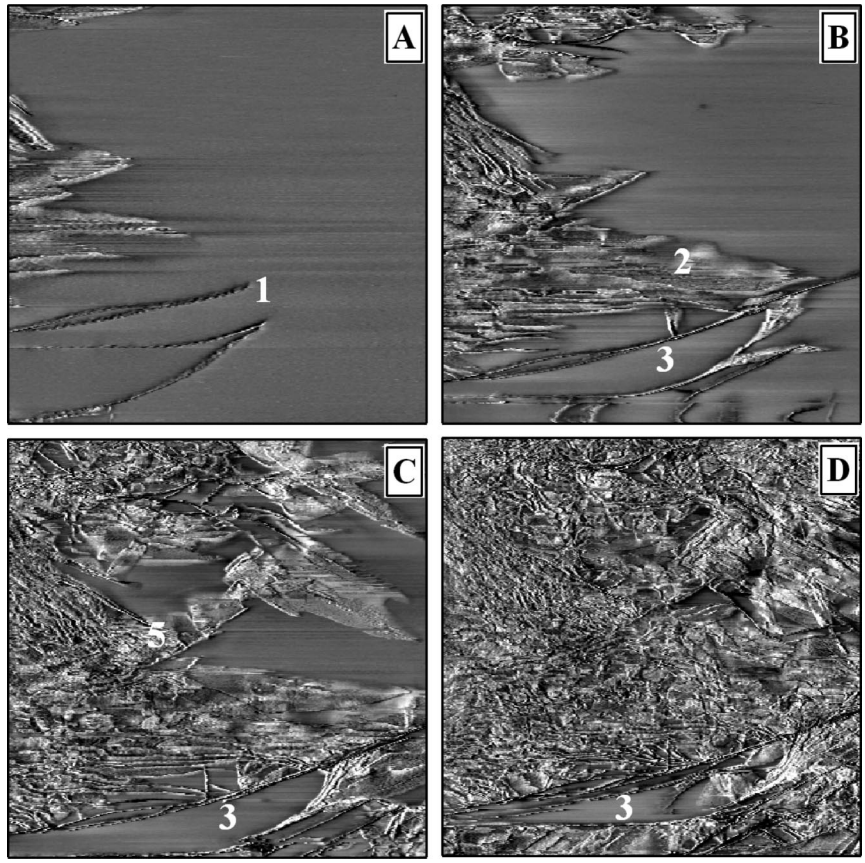

Figure 3. High-temperature tapping mode phase AFM images (8.0 × 8.0 μm^2) corresponding to the in situ melt-crystallization of PTT at 220 °C. The time lapse between the images is 8.5 min. Note the growing lamellae in the edge-on (1) and flat-on (2) orientations and a lake of amorphous material remaining after the passage of the main growth front (3).

resulting in helical ribbons, or helicoids. In the figure, the inclination of the lamella with respect to the surface continuously changes from a flat-on orientation at the top of the image to an almost edge-on near the lamellar tip. It is noteworthy that the growth rate at this temperature is still rather high for AFM imaging and, consequently, some deformations of the structural features may occur. Notwithstanding this technical difficulty, it is clear that the lamellae grow in stacks, in which the distance between the growing faces of the neighboring crystals in the direction of fast growth can be as large as one micrometer. The growth of lamellae lying closer to the surface seems to be delayed with respect to their neighbors deeper in the film. This effect could be accounted for by a slower diffusion of the amorphous material confined in a thin surface layer covering the lamella.

Another view of twisted PTT lamellae is given in Figure 2B. At such smaller scale, it can be seen that the edge-on oriented crystals exhibit regular stacking and are characterized by a significant lateral size. The beginning of the lamellar twist is visible in the bottom left corner of the image as a synchronous change in the direction defined by lamellar edges. The lamellae in this region cooperatively change their apparent direction. However, the real growth direction is not parallel to the lamellar edges because the lamellae have a shape of helicoidally twisted ribbons. Importantly, simultaneously with the variation of the their inclination in the plane of the image, the lamellae also tilt out of the image plane. This last effect is revealed by the increase in the apparent intercrystalline distance (long period) and also by the fact that the lamellar edges become less sharp in this part of the image.

It has been reported in the literature that at very high crystallization temperatures the morphology of PTT undergoes a change, where spherulites gradually loose their characteristic circular shape to become elliptic and eventually transform into axialites (cf. ref 28). A transition from a banded to nonbanded texture probably related to this change was observed here. To compare the lamellar growth for the two textures, AFM experiments were also performed at 220 °C, the results of which are shown in Figure 3. Lamellar tips growing in the edge-on (N1 in Figure 3A) and flat-on (N2 in Figure 3B) orientations can be clearly identified. Moreover, there is a pronounced difference in the local growth directions of the lamellae at the crystallization front. At the local scale, crystal growth is not uniform, and one even observes lakes of amorphous material (N3 in Figure 3C,D) left in the interior of the spherulite after the passage of the growth front. Solidification is significantly retarded in these regions. Such a growth mode agrees well with the optical images of the high-temperature axialites in the literature, where no radial orientation of the lamellae (absence of Maltese cross pattern) is observed which indicates a state of internal disorder.

III.2. SAXS/WAXS Experiments. The temperature program employed in the experiments included a short melting period at 250 °C followed by rapid cooling (−20 °C/min) to the isothermal crystallization temperature, T_c, (Figure 4). After isothermal crystallization the sample was heated at 5.0 °C/min up to the final melting point. The T_c of 205 °C was chosen because (i) it is the highest temperature at which isothermal crystallization advances at a reasonable pace and (ii) it is as close as possible to the temperature at which the *in situ* time-resolved crystallization experiments of the previous section were done.

Some of the unprocessed SAXS curves (i.e., not yet corrected for the scattering of the empty cell and the liquid-like back-

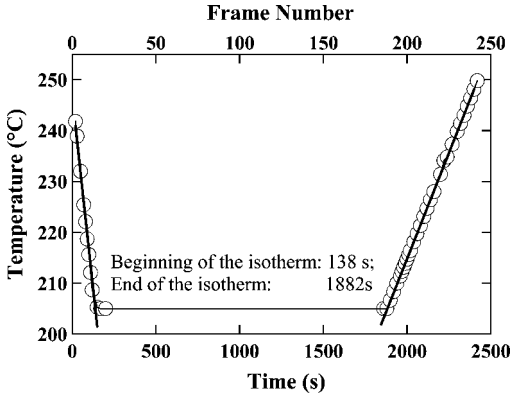

Figure 4. Temperature program used in the SAXS/WAXS experiment. Starting from the melt at 250 °C, the sample was cooled at 20 °C/min to the temperature of isothermal crystallization (205 °C). After completion of crystallization, the sample was heated to 250 at 5.0 °C/min. Heavy solid lines represent linear fits to the cooling and heating segment.

ground) are shown in Figure 5. Note that the crystallization process results in the appearance of the main interference maximum around 0.06−0.08 $Å^{-1}$ (Figure 5, left panel), which slightly shifts toward larger s-values. During heating of the isothermally crystallized sample (Figure 5, right panel), the interference maximum moves in the opposite direction and weakens as the melting process sets in. Averaged frames are displayed for the case of the isothermal crystallization, which explains why the data exhibits less scatter, especially at high s-values.

Selected processed SAXS curves are given together with the fits with the generalized paracrystalline stack model in Figure 6. After correction for the parasitic and liquid-like scattering, as well as the multiplication by the Lorentz factor the curves reveal more distinctly the second-order diffraction peak (visible as a shoulder at approximately 0.014−0.016 $Å^{-1}$) and a very faint broad ripple due to the form-factor of crystals with the first minimum (zero intensity point) at about 0.02 $Å^{-1}$. The existence of the ripple could be inferred only from some of the curves.

The SAXS curves corresponding to the later stage of crystallization could be successfully fitted using a large number of crystals per stack (e.g., $N = 20$). In this case, the fits become almost insensitive to N, which means that the paracrystalline stack appears to be virtually infinite. The situation with the first frames is qualitatively different, and good fits could only be obtained only with a very low value of N ($N = 3$).

In the course of heating, the SAXS intensity decreases with a simultaneous gradual shift toward lower s-values of the main maximum. Moreover an additional feature which looks like a shoulder at 223.1 °C, but later develops into a well-defined separate peak (cf. the curve at 223.9 °C) appears near $s = 0.004$ $Å^{-1}$. The ratio of the peak intensities gradually changes with temperature, and at about 225.6 °C, the low-s peak becomes more intense than the main peak.

The average values of the crystalline and amorphous thickness, $\langle L_c \rangle$ and $\langle L_a \rangle$, respectively, are given in Figure 7. As mentioned previously, the fits to the experimental curves with an infinite stack model are less successful at the onset of the isotherm and show some scatter. Therefore, the results obtained by using the structure factor of a paracrystalline stack with a very small height are considered to be more reliable. A decrease of the long period in the course of isothermal crystallization is a conventional observation in time-resolved SAXS experiments. In a previous publication a possible origin of this effect was attributed to an increase in average stack height.[14] Experimental evidence for a strongly increasing stack height during crystallization was found from high-temperature AFM imaging of PET during melt-crystallization.[21] In agreement with these results, one finds that in the case of PTT the use of a small-height stack sensitively reduces the $\langle L_a \rangle$ values at the beginning of crystallization (Figure 7).

The results corresponding to heating display a dramatic increase of $\langle L_a \rangle$ with temperature. Although $\langle L_a \rangle$ already noticeably changes shortly after the beginning of the heating ramp, the main variation occurs above approximately 222 °C when the sample enters the main melting region. In contrast, the crystal thickness hardly changes upon heating. As described elsewhere,[15] the crystals of PTT do not show much thickening on heating. It is even less so after crystallization of PTT at this high temperature, compared to previous observations made on PTT crystallized at 195 °C. It can thus be concluded that melting of PTT during heating occurs at an almost constant crystal thickness.

Further insights in the microstructural evolution of PTT during crystallization and melting can be gained from the analysis of the time- and temperature-dependence of the thickness distributions.

The results of the fits indicate that the parameters of the crystal thickness distribution are very different from those of the intrastack amorphous regions. The width of the crystal thickness distribution remains narrow at all times as usually found in the SAXS analysis of semicrystalline polymers.[29] The width of this distribution can, however, not be precisely determined from the fits. The main information must thus be extracted from the distributions of the intrastack amorphous regions illustrated in Figure 8.

In the course of isothermal crystallization (Figure 8, left) the amorphous layer thickness distributions hardly change. Although they exhibit some sharpening at later crystallization stages, the position of the maximum (i.e., the most probable value) remains nearly constant. This is at variance to what happens on heating (Figure 8, right). As shown in Figure 7, the amorphous thickness distributions undergo a drastic modification above 222 °C. In this case, the initially positively skewed distribution develops a clearly bimodal shape whereby the position of the first peak changes only slightly. Above approximately 224 °C, the bimodal shape of the distribution is no more detectable, as the first peak progressively disappears on heating, and all the distribution shifts to larger distances. Clearly in this temperature range most of the structural memory about the initial lamellar arrangement is erased by melting.

Selected WAXS curves measured during the same experiment are shown in Figure 9. Upon isothermal crystallization (left panel of Figure 9), the curves exhibit reflections characteristic of the triclinic unit cell of PTT.[30] The WAXS crystallinity index as a function of time clearly shows a rapid first stage and a slower logarithmic second stage. During heating (middle panel of Figure 9), the reflections weaken, however without any significant modification in their position or width. The temperature dependence of the crystallinity index, shown in the right panel of Figure 9, gives an estimate of the extent of melting.

III.3. Comparison of the Morphological Parameters of the Semicrystalline Structure Extracted from AFM and SAXS. A piece of complementary information on the microstructure of the PTT lamellar stacks can be obtained from AFM images measured in the regions where the lamellae are mainly oriented edge-on such as in Figure 10. The first examination of the structure reveals that, despite some defects in the lamellar arrangement and several remaining amorphous pockets, the lamellar stacking is very regular. Such perfect organization is quite striking for objects which are not flat and undergo a cooperative twist. Further studies would be required to under-

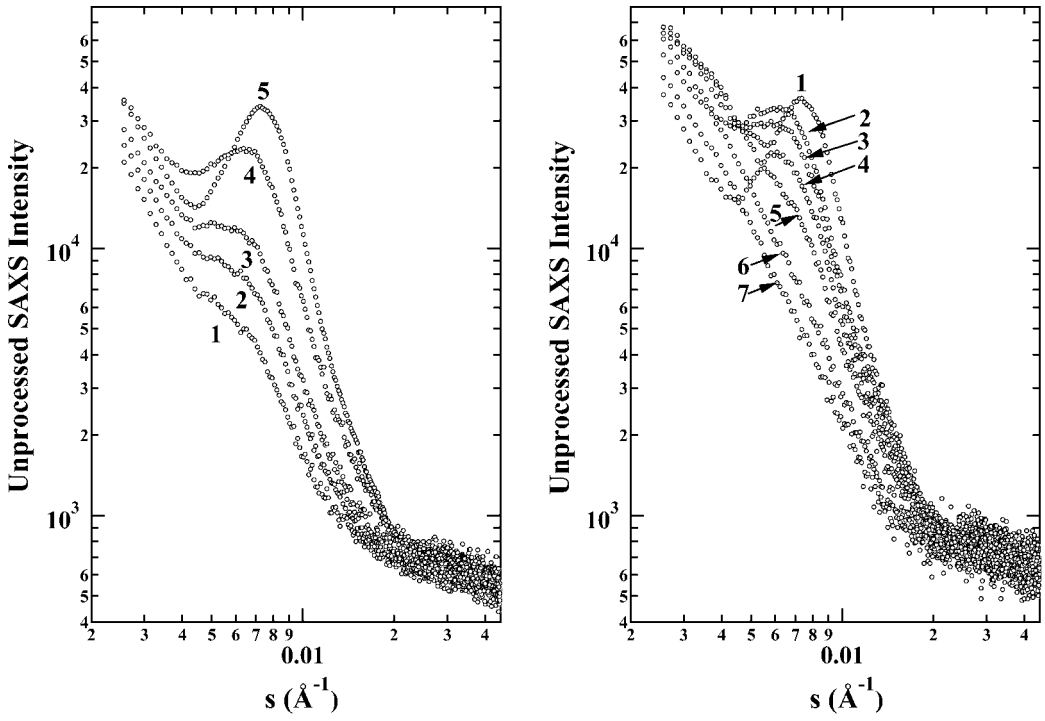

Figure 5. Unprocessed SAXS curves corresponding to an isothermal crystallization at 205 °C (left) and a subsequent heating ramp (right). Left: Elapsed crystallization times for the averaged frames are as follows: 1, 172 s; 2, 202 s; 3, 232 s; 4, 327 s; 5, 1727 s. Right: curves 1−7 correspond to temperatures of 210.7, 221.3, 222.2, 223.1, 223.9, 225.6, and 226.4 °C, respectively.

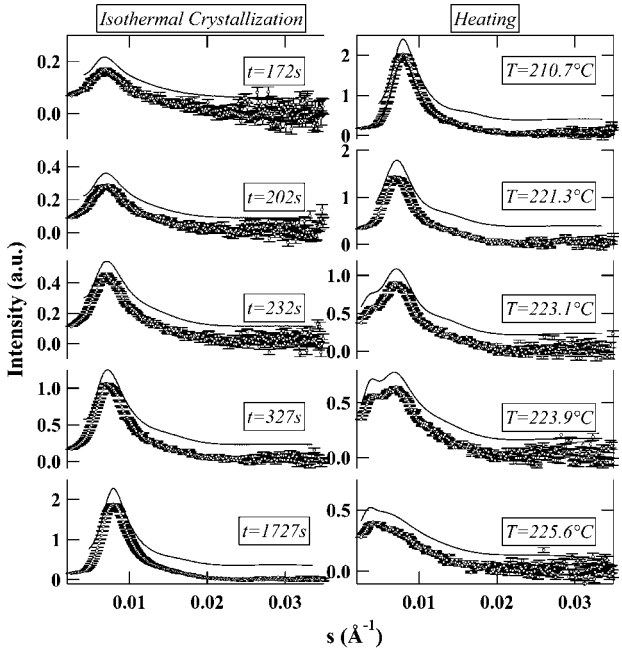

Figure 6. Processed SAXS curves ($s^2(I(s) - B)$ corresponding to isothermal melt-crystallization of PTT at 205 °C (left) and subsequent heating (right). The fits with the generalized paracrystalline model (solid lines) are offset vertically for clarity.

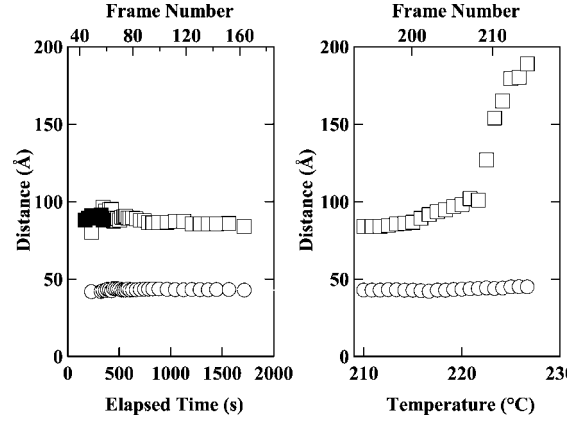

Figure 7. Average values of the crystal (circles) and amorphous layer (squares) thickness, $\langle L_c \rangle$ and $\langle L_a \rangle$, as a function of elapsed time at 205 °C (left) and temperature (right). Filled and empty squares correspond to the fits with a low ($N = 3$) and high ($N = 20$) number of crystals per stack, respectively.

stand in more depth the 3D shape of the lamellae and the way they self-organize during growth. The remaining amorphous pockets have sizes which typically do not exceed two or three long periods.

The bottom panel of Figure 10 depicts a lamellar stack constructed with a random number generator in accordance with the distributions of crystal and amorphous layer thickness found from the fits to the SAXS data as a barcode. The two figures are quite similar in terms of regularity of the lamellar positioning. However, the crystal thickness in the AFM image is noticeably larger. Both structures can be compared quantitatively in reciprocal and direct space, as shown in Figure 11. In the top panel, the analysis is performed in reciprocal space. To this end, the power spectral density function $P_1(s)$ (cf. eq 9) was computed from a fragment of the image in Figure 10, where the crystals are strictly oriented edge-on. The position of the $P_1(s)$ maximum can be directly compared to that of the SAXS curve measured at the end of the isotherm at 205 °C. The positions of the two maxima are in good agreement i.e. the long periods are close. However, the thickness distributions of the two regions reveal some discrepancies, as follows from the direct analysis (middle and bottom panels in Figure 11). AFM somewhat overestimates the crystal thickness and underestimates the thickness of the amorphous layer. The $\langle L_c \rangle$ from SAXS (4.3 nm) is about 30% smaller than the corresponding AFM value (5.6 nm). The situation is reversed for the average thickness of the amorphous layer: $\langle L_a \rangle$ from SAXS is 8.4 nm whereas AFM

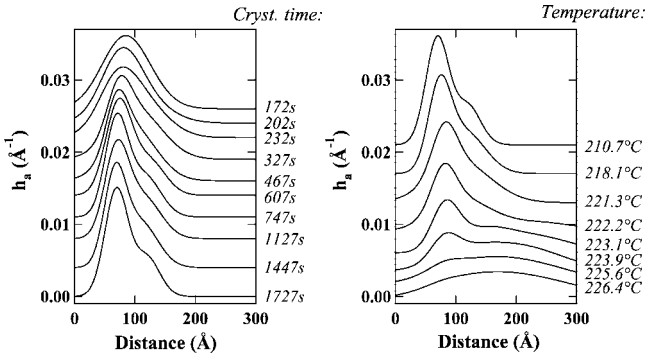

Figure 8. Normalized distributions of the intrastack amorphous regions for selected frames measured during isothermal crystallization at 205 °C (left) and subsequent melting during heating (right). The curves are offset vertically for clarity.

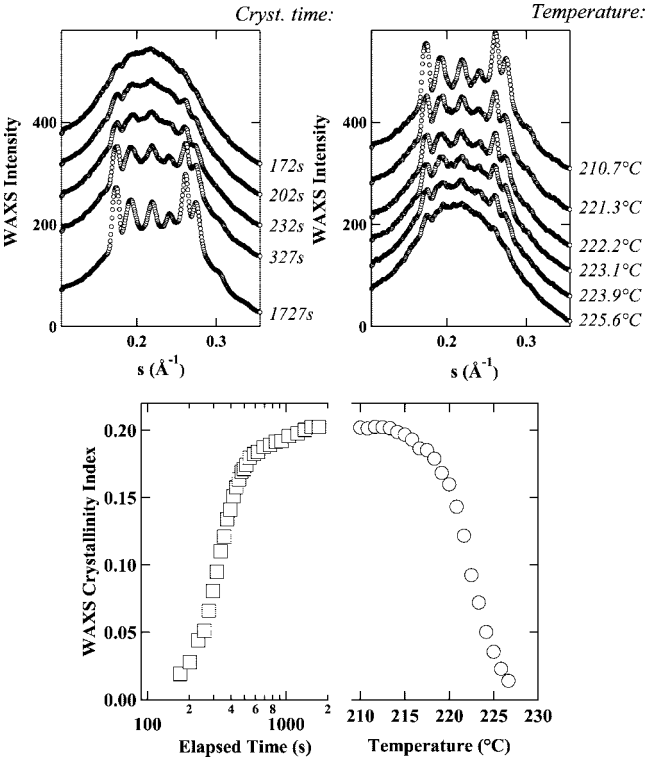

Figure 9. Selected frames showing the evolution of WAXS intensity for the isothermal crystallization at 205 °C (top left) and subsequent melting during heating (top right). The curves are offset vertically for clarity. The bottom panel displays the WAXS crystallinity index as a function of time for the isothermal crystallization (squares) and temperature (circles).

gives 6.0 nm. The discrepancy between the morphological parameters is likely to be due to the tip dilation effect, which is caused by the lamellar crystals being much harder than the devitrified interlamellar amorphous regions at this temperature. The tip penetrates deeper into the amorphous regions as can be illustrated by the corresponding topography images where the crystals protrude at the sample surface. This can account for the overestimation of the crystal thickness by AFM by about 1.3 nm.

IV. Discussion

IV.1. Semicrystalline Structure of the Melt-Crystallized PTT. The observed morphological parameters of PTT are typical of a low-crystallinity semirigid-chain polymer such as PEEK[31] or PET:[21,46] the PTT lamellae are thinner than the intrastack

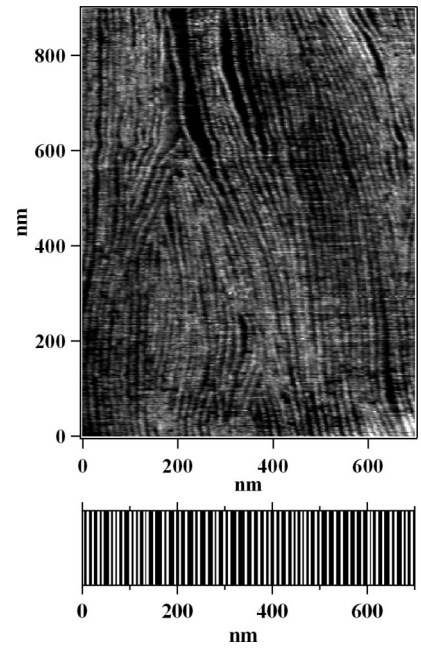

Figure 10. High-temperature tapping mode AFM image corresponding to the later stage of the *in situ* melt-crystallization of PTT at 210 °C. The bottom panel represents the semicrystalline structure formed at 205 °C, as viewed by SAXS. The structure was generated with a random number generator according to the Hosemann fit (see text for more details).

amorphous regions. Accordingly, the linear crystallinity determined by SAXS and AFM is below 50% even for the PTT samples crystallized at very high temperatures. Therefore the crystallinity of lamellar stacks is in general agreement with the overall bulk crystallinity, and there is no evidence for the inverted structure,[32] i.e. the one with thicker crystals and thin interlamellar amorphous regions. The morphological picture of PTT having thin lamellae is coherent with the absence of large amorphous pockets in the semicrystalline structure that were previously thought to compensate a hypothetically high linear crystallinity of the lamellar stack.[32]

A quantitative comparison between the results of AFM and SAXS shows that both techniques provide similar values of the long period. However, for AFM the analysis is complicated by the fact that only regions with edge-on oriented crystals can be analyzed. This problem does not exist for SAXS, as in this case the choice of the direction perpendicular to the lamellar surface is natural. A more detailed analysis of the thickness distributions of crystalline and amorphous regions from AFM images give distributions with shapes similar to those found from SAXS. The amorphous thickness distributions provided by both techniques exhibit a positive skew. The crystal thickness distribution from AFM is sharper than the distributions of amorphous regions. The rare occurrences of crystals thicker than 100 Å can be accounted for by the noise. On average, the crystal thickness is overestimated by AFM, which is an inherent problem of this technique related to the tip dilation. More work will be required to quantitatively correct the AFM values of the crystal thickness for example by the blind reconstruction method.[33]

IV.2. Evolution of the PTT Semicrystalline Structure during Heating. The access to the thickness distributions of crystalline and amorphous regions extracted from the fits with the paracrystalline stack opens the way to examine how the melting process occurs during heating of an isothermally crystallized PTT. In the Results Section, it was pointed out that melting mainly affects the amorphous regions. This is in line

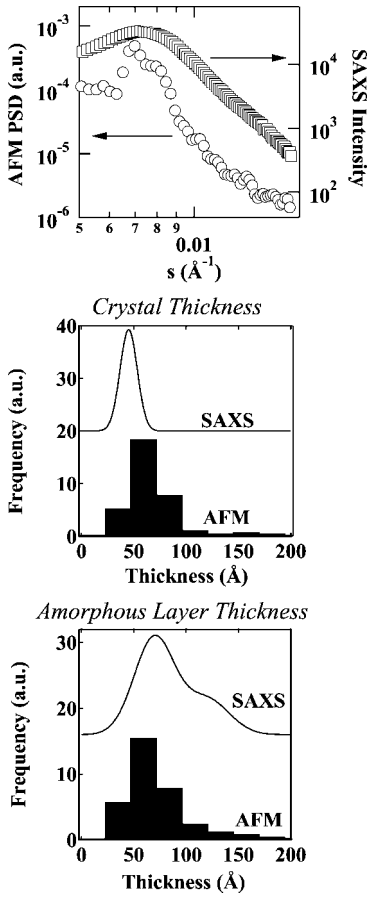

Figure 11. Comparison of the semicrystalline structure of PTT formed at 210 °C, as analyzed by SAXS and AFM. *Top*: SAXS curve measured at the end of the isotherm at 205 °C and power spectral density computed from a fragment of the AFM image in Figure 10. *Middle, Bottom*: distributions of crystals and interlamellar amorphous thickness extracted from the fit of the SAXS curve with the Hosemann model and computed from the AFM image in Figure 10.

with previous studies of melting of low-density polyethylene.[34] A simple model of random sequential melting has been proposed previously.[35] In this model, it is assumed that melting can be viewed as a sequence of uncorrelated melting events; i.e., the melting crystals are randomly selected in the lamellar stack. A rather straightforward consequence of this hypothesis is that melting will not modify the shape of the SAXS curve, except at the very end of melting where the scattering curve can be accounted for by scattering from isolated crystals, i.e., when the stacks are no longer present. We have previously shown that the random sequential melting model cannot explain the evolution of the distributions of amorphous regions observed in the experiment.[15] A qualitative manifestation of the discrepancy between the model and experiment can be easily observed in the present work: the SAXS curves exhibit a second low-s interference maximum at high temperatures, which was not initially present in the curves after the isothermal crystallization. This simple model clearly does not reproduce the real melting process in PTT.

To analyze the mechanisms of melting, it is convenient to compute differential distribution functions ($\Delta h_{a,T}$) defined as follows:

$$\Delta h_{a,T} = \frac{1}{\alpha_c(T_0)}(\alpha_c(T+\Delta T)h_{a,T+\Delta T} - \alpha_c(T)h_{a,T}) \qquad (10)$$

where $h_{a,T}$ and $\alpha_c(T)$ are the thickness distribution of amorphous regions and WAXS crystallinity index corresponding to temperature T, respectively. The $\alpha_c(T_0)$ stands for the crystallinity

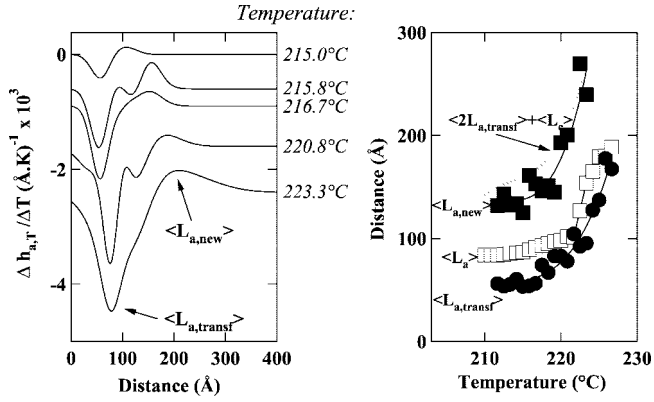

Figure 12. Evolution of the thickness distributions of amorphous layers during heating. *Left*: Differential distribution functions (see text) showing negative and positive peaks corresponding to the amorphous regions that disappear ($\langle L_{a,transf}\rangle$) and appear ($\langle L_{a,new}\rangle$) in the semicrystalline structure, respectively. The curves are offset vertically for clarity. *Right*: temperature dependence of the average thickness of amorphous regions $\langle L_{a,transf}\rangle$ and $\langle L_{a,new}\rangle$. Solid lines are guides for the eye. Dotted line indicates a theoretical thickness of the amorphous region generated following the melting of a PTT crystal surrounded by two amorphous regions equal to $\langle L_{a,transf}\rangle$ (i.e., 2 $\langle L_{a,transf}\rangle$ + $\langle L_c\rangle$). The $\langle L_{a,transf}\rangle$ is systematically smaller than $\langle L_a\rangle$, which indicates that melting mainly affects the crystals squeezed between two thin amorphous layers ($\langle L_{a,transf}\rangle$).

index at the end of the isothermal crystallization at T_0 (205 °C in the present case). Equation 10 renormalizes the thickness distributions according to the corresponding crystallinity index determined by WAXS. The physical meaning of this renormalization is obvious: in a semicrystalline structure composed of thick lamellar stacks the number of interlamellar amorphous regions equals the number of crystals. To visualize the changes in the distribution of amorphous regions as a function of temperature, one has first to make them scale to the total number of crystals present in the structure, for example to the corresponding α_c. This number was taken to have a value of one at the end of the isotherm.

The differential distributions of amorphous regions are exemplified in the left panel of Figure 12. From the definition in eq 10, it is clear that the position of a negative peak in the differential distributions corresponds to the amorphous regions that disappear at a particular temperature, whereas the positive peak reflects the amorphous regions appearing in the structure. In absence of recrystallization, the size of the disappearing amorphous regions should obviously be smaller than that of those newly appearing. It is useful to compute the first moments of the differential distributions (i.e., the average sizes). In this case, for example the integral $\int_{l_1}^{l_2} \Delta h_{a,T}(l)\, dl$ gives the number fraction of amorphous regions ranging from l_1 to l_2, which disappear (if negative) or appear (if positive) between T and $T + \Delta T$. The average sizes of the disappearing ($\langle L_{a,transf}\rangle$) and appearing ($\langle L_{a,new}\rangle$) amorphous regions are plotted as a function of temperature in the right panel of Figure 12. The values of $\langle L_{a,transf}\rangle$ are smaller than the average size of amorphous regions $\langle L_a\rangle$. The melting process is thus clearly not random, but mainly affects the population of the thinnest amorphous regions.

Note that the size of the newly formed amorphous regions is not very different from $2\langle L_{a,transf}\rangle + \langle L_c\rangle$ (dotted line in Figure 12, right), which means that the majority of the melting PTT crystals are squeezed between two thin amorphous regions having a thickness of $\langle L_{a,transf}\rangle$. Interestingly, such confinement-driven melting continues even at temperatures where the values of $\langle L_{a,transf}\rangle$ become comparable to the $\langle L_{a,new}\rangle$ values corresponding to the onset of melting. In this case melting cannot be considered anymore as melting of single crystals in a stack

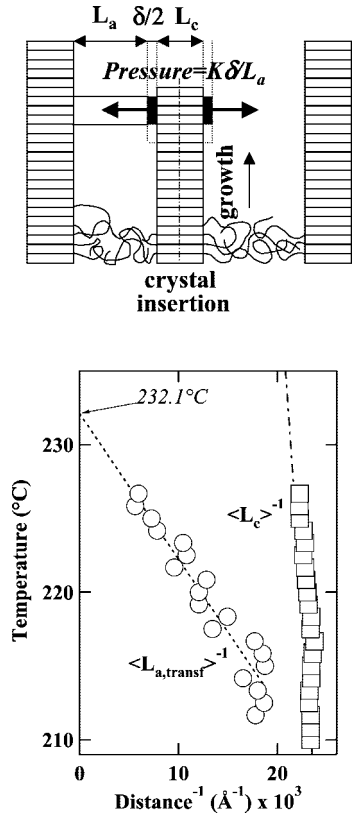

Figure 13. *Top*: cartoon showing the origin of negative pressure exerted on a lamellar crystal growing within the scaffold of the dominant lamellae. The interconnection of the chains pertinent to the crystal and amorphous regions is accounted for by a low concentration of chain folds at the crystal surface. *Bottom*: Temperature dependence of the reciprocal distances $\langle L_{a,transf}\rangle$ and $\langle L_c\rangle$. The conventional evaluation of the thermodynamic melting temperature from the linear extrapolation of the temperature variation of $\langle L_c\rangle^{-1}$ toward the intersection with the ordinate (dashed-dotted line) gives an unrealistically high value. The values of $\langle L_{a,transf}\rangle^{-1}$ scale linearly with temperature showing that the melting temperature of PTT crystals is affected by the size of the neighboring amorphous regions. The extrapolation of the line **T** versus $\langle L_{a,transf}\rangle^{-1}$ gives the melting temperature of PTT crystals, which are not confined by neighboring amorphous regions.

because a large fraction of melting crystals now have missing (i.e., molten) neighbors.

Importantly, heating of PTT hardly brings about any lamellar thickening: the L_c stays almost constant till the very end of melting. The possibility that the effect described above is only due to the thinner PTT crystals melting first can be ruled out. It can thus be concluded that the thickness of amorphous regions bordering the crystalline lamella affects its thermal stability.

IV.3. Thermal stability of the PTT Crystals. In the previous section, the impact of confinement on melting of the PTT crystals was analyzed, based on the temperature evolution of the thickness distributions of amorphous regions. A possible explanation for this effect is proposed in Figure 13 (top panel). The cartoon depicts a lamellar stack with uneven growth front, as observed by time-resolved AFM. The later growth of one of the crystals occurs within the scaffold of the already grown dominant lamellae. This is in agreement with well-established morphological schemes of rapidly growing dominant lamellae and in-filling subsidiary lamellae suggested previously for other semirigid chain polymers such as PEEK.[31,36]Since the growth of a subsidiary lamella is accompanied by a densification of the lamellae core, it results in the buildup of stresses exerted on the growing crystal by the amorphous phase. One of the factors impeding the rapid relaxation of stresses at the lamellar tip is the high viscosity of the PTT melt and its confinement within a narrow interlamellar gap. Another factor is the particular structure of the crystal/amorphous interphase common to all semirigid chain polymers. It is generally admitted that, for these polymers, the crystalline core is intimately linked to the amorphous region by a flux of chains emanating from the crystal surface. Accordingly, a reduction in the fraction of folds at the surface of semirigid chain crystals was previously shown in computer simulations using the Bragg-Williams mean-field approximation.[37,38]

The negative pressure P exerted on the lamella due to the densification can be roughly estimated from the deformation of the amorphous layer (δ) accompanying crystallization:

$$P = K\frac{\delta}{L_a} \tag{11}$$

where K stands for the bulk modulus, which is related to the Young modulus via the Poisson coefficient.[39] The value of δ can thus be written as:

$$\delta = L_c\frac{\rho_c - \rho_a}{\rho_a} \tag{12}$$

where ρ_c and ρ_a stand for the density of the crystalline and amorphous phase, respectively. The influence of a negative pressure on the melting temperature can be estimated using the Clapeyron-Clausius equation:

$$\frac{dT}{dP} = T\frac{\Delta V_{tr}}{\Delta H_{tr}} \tag{13}$$

where ΔV_{tr} and ΔH_{tr} denote the volume and enthalpy changes resulting from the phase transition. By substituting eqs 11 and 12 into eq13, one obtains the expression for the melting point depression ΔT:

$$\Delta T = KT\frac{L_c}{L_a}\frac{\rho_c - \rho_a}{\rho_a}\frac{\Delta V_{tr}}{\Delta H_{tr}} \tag{14}$$

It can be further modified as

$$\Delta T = \frac{1}{L_a}\left[\frac{KTL_c}{\Delta H_{tr}}\frac{(\rho_c - \rho_a)^2}{\rho_c\rho_a^2}\right] \tag{15}$$

From eq 15 it follows that ΔT should be proportional to the reciprocal size of the amorphous region adjacent to the crystal. The experimental data displayed in Figure 13 (bottom panel) illustrates that, indeed, the melting temperature scales linearly with $\langle L_{a,transf}\rangle^{-1}$. The dotted line in the figure is a fit with the expression:

$$T = T_0 - \frac{C}{L_{a,transf}} \tag{16}$$

where C is approximately 1×10^3 K Å. If one substitutes this value into eq 14 ($C = \Delta TL_a$), together with the literature data for PTT, $\rho_c = 1.427$ g/cm^3,[40] $\rho_a = 1.305$ g/cm^3[41] and $\Delta H_{tr} =$ 30 kJ/mol,[42] the resulting bulk modulus K is 1.1 GPa. This is on the same order of magnitude as for example the corresponding value for polyisoprene (~2 GPa).[43] Since K is not a very material-sensitive property this agreement can be considered satisfactory.

It is worth noting that the coordinates of Figure 13 are identical to those used for the Gibbs−Thomson equation, which expresses the melting point depression as a function of crystal thickness. The reciprocal crystal thickness of PTT is plotted on the same graph (open squares). A linear fit through these points gives an unrealistically high equilibrium melting point of PTT (437 °C), which exceeds by far the literature values of 237[42,44] and 248 °C.[45] In the context of the model this line does not correspond to the real correlation between the melting temper-

ature and crystal thickness, however, because the latter remains essentially constant during heating. Instead, the temperature dependence of the thickness of amorphous regions expresses the melting point depression caused by the crystal confinement. By taking the rough estimate of K obtained above, it follows that, at the end of the isotherm at 205 °C, the crystals are subject to a negative pressure of about 50 MPa. This pressure lowers their melting point by approximately 20 °C. The gradual increase of the amorphous layer thickness with temperature continuously shifts the melting point of the crystals upward. This happens practically in absence of any crystal thickening. Extrapolation of the T *versus* $\langle L_{a,transf}\rangle^{-1}$ line to the intersection with the vertical axis (227.1 °C) gives the highest possible melting point of a PTT crystal with a thickness of 4.5 nm. This temperature thus corresponds to the melting point of a PTT crystal in absence of any constraints due to the neighboring amorphous regions ($\langle L_{a,transf}\rangle^{-1} \rightarrow 0$). Such crystals were not observed experimentally but the possibility of having a system of remaining sparse crystals, which scatter independently, is expected theoretically.

V. Conclusions

Analysis of time- and temperature-resolved SAXS measurements corresponding to an isothermal melt-crystallization of PTT at 205 °C and a subsequent linear heating ramp has been performed using the generalized paracrystalline lamellar stack model. The results of the fits corresponding to the isothermal crystallization are in general agreement with the morphological parameters of the PTT semicrystalline structure obtained from high-temperature AFM imaging.

The SAXS data analysis indicates that the crystal thickness remains almost constant throughout the isothermal crystallization and melting. The size-distributions of the interlamellar amorphous regions exhibit only small variations during isothermal crystallization, whereas they change dramatically across the melting transition. Examination of the differential size-distribution functions normalized by the WAXS crystallinity index reveals that the crystals squeezed between the thinnest amorphous layers melt first. The reciprocal size of the amorphous regions undergoing transformation scales linearly with temperature. Given the uniformity of the crystal population, it is thus clear that the melting point of the crystals does not solely depend on their thickness but is affected by the adjacent amorphous regions. A simple model is proposed, which accounts for this confinement-driven melting by a negative pressure imposed on the crystals by the neighboring amorphous regions. A pressure of 50 MPa is estimated from the Clapeyron−Clausius equation for the crystals melting just above the isothermal crystallization temperature. During melting, the constraints on the crystals gradually relax, which increases the melting point of the remaining crystals. This can explain why the melting region of PTT and, more generally, that of the semirigid chain semicrystalline polymers, is broad, while the crystal thickness exhibits only limited variation.

Acknowledgment. D.A.I. acknowledges the gift of the PTT samples by Shell Co., as well as technical support and fruitful discussions with M. Buscemi (Shell Coordination Center, Louvain-la-Neuve, Belgium) and H. H. Chuah and K. Kiibler (Westhollow Technology Center, Shell Chemical Company, Houston, TX). The authors acknowledge S. Hocquet for the help with the SAXS experiments.

References and Notes

(1) Lee, Y.; Porter, R. S. *Macromolecules* **1987**, *20*, 1336.
(2) Lee, Y.; Porter, R. S.; Lin, J. S. *Macromolecules* **1989**, *22*, 1756.
(3) Holdsworth, P. G.; Turner-Jones, A. *Polymer* **1971**, *12*, 195.
(4) Fougnies, C.; Damman, P.; Dosière, M.; Koch, M. H. J. *Macromolecules* **1997**, *30*, 1392.
(5) Ivanov, D. A.; Jonas, A. M.; Legras, R. *Polymer* **2000**, *41*, 3719.
(6) Ivanov, D. A.; Jonas, A. M. *Macromolecules* **1998**, *31*, 4546.
(7) Dupont, O.; Jonas, A. M.; Nysten, B.; Legras, R.; Adriensens, P.; Gelan, J. *Macromolecules* **2000**, *33*, 562.
(8) Pyda, M.; Boller, A.; Grebowicz, J.; Chuah, H.; Lebedev, B. V.; Wunderlich, B. *J. Polym. Sci.: Part B: Polym. Phys.* **1998**, *36*, 2499.
(9) (a) Yang, J.; Sidoti, G.; Liu, J.; Geil, P. H.; Li, C. Y.; Cheng, S. Z. D. *Polymer* **2001**, *42*, 7181. (b) Chung, W. T.; Yeh, W. J.; Hong, P. D. *J. Appl. Polym. Sci.* **2002**, *83*, 2426.
(10) Wang, B. J.; Li, C. Y.; Hanzlicek, J.; Cheng, S. Z. D.; Geil, P. H.; Grebowicz, J.; Ho, R. M. *Polymer* **2001**, *42*, 7171.
(11) (a) Wu, J.; Schultz, J. M.; Samon, J. M.; Pangelinan, A. B.; Chuah, H. H. *Polymer* **2001**, *42*, 7141. (b) Wu, J.; Schultz, J. M.; Samon, J. M.; Pangelinan, A. B.; Chuah, H. H. *Polymer* **2001**, *42*, 7161.
(12) (a) Ruland, W. *Colloid Polym. Sci.* **1977**, *255*, 417. (b) Strobl, G. R.; Schneider, M. *J. Polym. Sci.* **1980**, *18*, 1343.
(13) Hosemann,R. Bagchi S. N. *Direct Analysis of Diffraction by Matter*; North Holland: Amsterdam, 1962.
(14) Ivanov, D. A.; Legras, R.; Jonas, A. M. *Macromolecules* **1999**, *32*, 1582.
(15) Ivanov, D. A.; Hocquet, S.; Dosière, M.; Koch, M. H. J. *Eur. Phys. J. E* **2004**, *13*, 363.
(16) Koch, M. H. J.; Bordas, J. *Nucl. Instrum. Methods* **1983**, *208*, 435.
(17) (a) Boulin, C. J.; Kempf, R.; Gabriel, A.; Koch, M. H. J. *Nucl. Instrum. Methods* **1988**, *A269*, 312. (b) Rapp, G.; Gabriel, A.; Dosière, M.; Koch, M. H. J. *Nucl. Instrum. Methods* **1995**, *A357*, 178.
(18) Konarev, P. V.; Volkov, V. V.; Sokolova, A. V.; Koch, M. H. J.; Svergun, D. I. *J. Appl. Crystallogr.* **2003**, *36*, 1277.
(19) Wilson, A. J. C., Prince, E., Eds. *International Tables for Crystallography*; Kluwer Academic Publishers: Dordrecht, The Netherlands, 1999; p 236 ff.
(20) Ivanov, D. A.; Daniels, R., Magonov, S. N. *Exploring the High-Temperature AFM and Its Use for Studies Polymers* Application Note published by Digital Instruments/Veeco Metrology Group February, **2001**.
(21) Ivanov, D. A.; Amalou, Z.; Magonov, S. N. *Macromolecules* **2001**, *34*, 8944.
(22) Press, et al. *Numerical Recipes in C, The Art of Scientific Computing*. Plenum Press: New York, 1988.
(23) Balta-Calleja,J. F.; Vonk C. G. *X-ray Scattering of Synthetic Polymers"*.Elsevier: Amsterdam, 1989.
(24) Basire, C.; Ivanov, D. A. *Phys. Rev. Lett.* **2000**, *85*, 5587.
(25) Ivanov, D.A. Magonov S. Atomic Force Microscopy Studies of Semicrystalline Polymers at Variable Temperature In *Polymer Crystallization: Observations Concept and Interpretations*edt bySommer J. U., Reiter,G., Eds.; Springer-Verlag: Berlin, 2003; pp 98−129.
(26) Basiura, M.; Gearba, R. I.; Ivanov, D. A.; Janicki, J.; Reynaers, H.; Groeninckx, G.; Bras, W.; Goderis, B. *Macromolecules* **2006**, *39*, 8399.
(27) Press, W. H.; et al. *Numerical Recipes in C, The Art of Scientific Computing*; Plenum Press: New York, 1988).
(28) Chuang, W.-T.; Hong, P.-D.; Chuah, H. H. *Polymer* **2004**, *45*, 2413.
(29) Al-Hussein, M.; Strobl, G. *Eur. Phys. J. E* **2001**, *6*, 305.
(30) Poulin-Dandurand, S.; Pérez, S.; Revol, J. F.; Brisse, F. *Polymer* **1979**, *20*, 419.
(31) Blundell, D. J.; Osborn, B. N. *Polymer* **1983**, *24*, 953.
(32) Verma, R. K.; Hsiao, B. S. *Trends Polym. Sci.* **1996**, *4*, 312.
(33) Villarrubia, J. S. *J. Res. Natl. Inst. Stand. Technol.* **1997**, *102*, 425.
(34) Strobl, G. R.; Schneider, M. J.; Voigt-Martin, I. G. *J. Polym. Sci. Polym. Phys. Ed.* **1980**, *18*, 1361.
(35) Crist, B. *J. Polym; Sci.: Part B: Polym. Phys.* **2001**, *39*, 2454.
(36) Olley, R. H.; Bassett, D. C.; Blundell, D. J. *Polymer* **1986**, *27*, 344.
(37) Kumar, S. K.; Yoon, D. Y. *Macromolecules* **1989**, *22*, 4098.
(38) Kumar, S. K.; Yoon, D. Y. *Macromolecules* **1991**, *24*, 5414.
(39) Ward, I M. , *Mechanical Properties of Solid Polymers*; Wiley Interscience: London, 1971.).
(40) Desborough, I. J.; Hall, I. H.; Neisser, J. Z. *Polymer* **1979**, *20*, 545.
(41) Lee, H. S.; Park, S. C.; Kim, Y. H. *Macromolecules* **2000**, *33*, 7994.
(42) Pyda, M. *J. Polym. Sci., Part B: Polym. Phys.* **1998**, *36*, 2499.
(43) Brandrup, J.; Immergut, E. H. *Polymer Handbook*, 3rd ed.; John Wiley & Sons: New York, 1989.
(44) ATHAS Databank available online: http://web.utk.edu/~athas/databank/phenylen/ptt/ptt.html.
(45) Huang, J.-M.; Chang, F. C. *J. Polym. Sci., Part B: Polym. Phys.* **2000**, *38*, 934.
(46) The existence of such amorphous regions perturbed by the nearby crystalline surfaces was recently demonstrated for a binary blend of similar semi-rigid chain aromatic polyester with TEM using selective staining: Ivanov, D. A.; Pop, T.; Yoon, D. *Macromolecules* **2002**, *35*, 9813.

MA801604A